

---

# Hierarchical Symbolic Reasoning in Hyperbolic Space for Deep Discriminative Models

---

Ainkaran Santhirasekaram\* †  
a.santhirasekaram19@ic.ac.uk

Avinash Kori\* †  
a.kori21@ic.ac.uk

Andrea Rockall ‡  
a.rockall@ic.ac.uk

Mathias Winkler ‡  
m.winkler@ic.ac.uk

Francesca Toni †  
f.toni@ic.ac.uk

Ben Glocker †  
b.glocker@ic.ac.uk

\* joint first author

† Department of Computing, Imperial College London

‡ Department of Surgery and Cancer, Imperial College London

## Abstract

Explanations for *black-box* models help us understand model decisions as well as provide information on model biases and inconsistencies. Most of the current explainability techniques provide a single level of explanation, often in terms of feature importance scores or feature attention maps in input space. Our focus is on explaining deep discriminative models at *multiple levels of abstraction*, from fine-grained to fully abstract explanations. We achieve this by using the natural properties of *hyperbolic geometry* to more efficiently model a hierarchy of symbolic features and generate *hierarchical symbolic rules* as part of our explanations. Specifically, for any given deep discriminative model, we distill the underpinning knowledge by discretisation of the continuous latent space using vector quantisation to form symbols, followed by a *hyperbolic reasoning block* to induce an *abstraction tree*. We traverse the tree to extract explanations in terms of symbolic rules and its corresponding visual semantics. We demonstrate the effectiveness of our method on the MNIST and AFHQ high-resolution animal faces dataset. Our framework is available at <https://github.com/koriavinash1/SymbolicInterpretability>.

## 1 Introduction

Explainable AI (XAI) aims to improve the transparency and trustworthiness of deep learning models [1, 2]; XAI can help with identifying biases, which is important for the safe and fair use of prediction models [3]. XAI approaches can be broadly categorized into ante-hoc and post-hoc methods [4]. Ante-hoc explainability focuses on developing inherently transparent models. For example, [5] introduces a symbolic reasoning block to promote transparency during training while [6] uses natural language descriptions that complement model predictions. [7] develops intrinsically aligned models via a debating game with a human judge.

Post-hoc explanations are the most commonly explored approaches, including explanations via feature-attribution [8, 9, 10], saliency maps [11, 12, 13] counterfactuals [14] or concept extraction [15, 16, 17]. Feature attribution methods [8, 9] focus on assigning importance weighting to each and every feature in an input space, indicating their contribution towards the classifier’s decision; these methods are also considered shallow example-based explanations as they do not provide any further feedback on the model. Saliency-based methods [11] generate attention maps in an

input space indicating regions responsible for deriving the classifier’s decision. These methods also provide example-based explanations. However, both feature-attribution and saliency-based explanations do not highlight the model’s perceived feature interactions as they only work on input data, which makes explanations a function of the data as well as of the model. This makes it difficult to assess the faithfulness of explanations towards the model’s reasoning. Counterfactual explanation methods [18, 19, 20, 21] help in analysing a classifier by creating several carefully constructed *what-if* scenarios by perturbing specific features, but are also example-based.

These methods overall provide single stage explanations but do not consider concept-based reasoning as perceived by humans [22, 23]. Concept-based explanations [15, 16, 17] go beyond feature-attribution and saliency-based methods by constructing higher-level concepts indicating their influence on the classifier’s decision. [17, 16] focus on developing traces, which indicate the flow of reasoning to make certain predictions, thereby considering feature interaction. These approaches are closely related to a popular wave of AI termed neuro-symbolic learning [24, 25, 26, 27], where a data-driven deep learning method is used to learn sub-symbolic representations to denote concepts while exploiting symbolic methods to capture reasoning. In fact, studies in computational neuroscience have claimed that concept representation in the brain can be in a finite discrete form rather than using continuous and infinitely many representations [28].

The notion of hierarchical concept-based reasoning is the most commonly posited learning principle in systems neuroscience [23, 29, 30, 31]. This form of reasoning has already been employed in neuro-symbolic AI [32, 33] to develop hierarchical representations in the form of knowledge/abstractions graphs and induce hierarchical rules as explanations. However these approaches are limited in developing hierarchical visual reasoning for classification tasks due to a continuous latent space. They do not also consider the natural geometry of the space upon which to develop hierarchical or neuro-symbolic models.

Inspired by hierarchical reasoning, we tackle the aforementioned issues to develop hierarchical symbolic explanations for deep discriminative models trained on imaging data. Our approach distills the knowledge from a trained classifier into a discrete surrogate model. We consider the natural geometry in which to develop our discrete surrogate model and form a hierarchical symbolic representation in hyperbolic space of the visual world with the learned interactions between symbols forming an abstraction tree [34]. This method makes generated explanations faithful to the classifier rather than the data. It also addresses the issue of non-monotonic behavior of features, by considering discrete symbols which can either be sampled or not. Our main contributions in this work include:

- **Symbol formation (Sections 3.2, 3.3):** A method to discretise the continuous latent space of a given classifier model into a hierarchy of discrete vectors denoted as symbols. We exploit the natural structure of hyperbolic geometry to more efficiently model this hierarchy.
- **Symbol abstraction and hyperbolic reasoning module (Section 3.3):** An effective way of learning symbol conjunction using binary weight layers to form an abstraction tree, which can provide both local image-level and global class-level hierarchical rules.
- **Explanations (Section 3.4):** A way of obtaining visual semantics for any given symbol in a hierarchy.

## 2 Background

**Vector quantisation:** [35] proposed a new way of training variational autoencoders (VAE) with discrete latent variables, which showed competitive performance with its continuous counterparts. They achieve the discretisation of the continuous latent variables from the output of an encoder with a method called vector quantisation (VQ). We therefore use VQ to learn a set of discrete symbols to represent the continuous latent space of a classifier.

**Hyperbolic embeddings:** A natural objective when embedding symbolic data in graphs is for the distances between symbols, defined by the space which they reside in, to correlate with their semantic similarity. However, to model increasingly complex relations between symbols, one is bounded by the dimensionality of embeddings in Euclidean space [36]. This is because the number of nodes in most cases grows exponentially as the graph distance from the centre node increases, while Euclidean space grows polynomially. This leads to embedding distortion and loss of information [37]. Hyperbolic geometry is a form of non-Euclidean geometry with a constant negative Gaussian



The **Riemannian Metric** defines the set of inner products  $g_x : \mathcal{T}_x \mathcal{M} \times \mathcal{T}_x \mathcal{M} \rightarrow \mathbb{R}$  of every point  $x$  on  $\mathcal{M}$ . **Parallel transport**  $P_{x \rightarrow y}$  describes the translation of a vector field  $V$  along a differentiable manifold to a new vector field  $V'$  such that the covariant derivative always stays at 0.

We now introduce the **Hyperboloid** and **Poincare** models of hyperbolic space equipped with constant negative curvature  $-1/K$ , ( $K > 0$ ). In the rest of this works, we work with only hyperboloid  $\mathbb{H}^{d,K}$  and Poincare  $\mathbb{B}^{d,K}$  models of  $d$  dimensions with unit radius and hence fixed negative curvature of  $-1$ ;  $\mathbb{H}^{d,1}$ ,  $\mathbb{B}^{d,1}$ . We focus on the two sheet unit hyperboloid model defined by Riemmanian metric  $g_x^{\mathbb{H},1}$  given by the Minkowski metric tensor  $\langle \cdot, \cdot \rangle_S$  whereby  $\langle x, x \rangle_S = -1$  and  $x \in \mathbb{R}^{d+1}$  [40]. Therefore, the dot product between arbitrary points  $u$  and  $v$  on  $\mathbb{H}^{d,1}$ , is defined as  $g_x^{\mathbb{H},1} \langle u, v \rangle := -u_0 v_0 + u_1 v_1 \dots + u_d v_d$ ;  $u_0 > 0$  [40]. Given the definition of the Riemannian metric tensor, we can introduce the notion of the geodesic distance defined as the shortest distance between  $(u, v) \in \mathbb{H}^{d,1}$ . Geodesic distance in the hyperboloid is given as in [40]:  $d^{\mathbb{H},1}(u, v) = \text{arcosh}(g_x^{\mathbb{H},1} \langle u, v \rangle)$ .

We next formally define the Poincare unit ball,  $\mathbb{B}^{d,1} = \{x \in \mathbb{R}^d \mid \|x\| < 1\}$ . Geodesics in  $\mathbb{B}^{d,1}$  are arcs of circles orthogonal to the boundary.  $\mathbb{B}^{d,1}$  is determined by the following Riemmanian metric tensor:  $g_x^{\mathbb{B},1} = \left( \frac{2}{1-\|x\|^2} \right)^2$ . This allows to define the geodesic distance for  $(u, v) \in \mathbb{B}^{d,1}$  below:

$$d^{\mathbb{B},1}(u, v) = 1 + 2 \left( \frac{\|u - v\|^2}{(1 - \|u\|^2)(1 - \|v\|^2)} \right) \quad (1)$$

Now we introduce the notion of mapping between hyperbolic and euclidean space (tangential plane). Given  $y \in \mathcal{T}_x \mathbb{H}^{d,1}$  and  $v \in \mathbb{H}^{d,1}$ , exponential and logarithmic mappings are denoted  $\text{exp}_x^{\mathbb{H},1}(y) : \mathcal{T}_x \mathbb{H}^{d,1} \rightarrow \mathbb{H}^{d,1}$  and  $\text{log}_x^{\mathbb{H},1}(v) : \mathbb{H}^{d,1} \rightarrow \mathcal{T}_x \mathbb{H}^{d,1}$  respectively. In this work, we perform mappings with the tangential space at the origin  $o$ , which for  $\mathbb{H}^{d,1}$  is defined on  $\{1, 0_1, \dots, 0_d\} \in \mathbb{H}^{d,1}$ . In this case, the mappings between  $y \in \mathcal{T}_o \mathbb{H}^{d,1}$  and  $v \in \mathbb{H}^{d,1}$  such that  $\langle y, o \rangle = 0$  are calculated as follows:

$$\text{exp}_o^{\mathbb{H},1}(y) = \left( \cosh(\|y_{1:d}\|_2), \sinh(\|y_{1:d}\|_2) \frac{y_{1:d}}{\|y_{1:d}\|_2} \right); \text{log}_o^{\mathbb{H},1}(v) = \left( 0, \text{arcosh}(v_0) \frac{v_{1:d}}{\|v_{1:d}\|_2} \right) \quad (2)$$

Next, the equations for the mappings between  $y$  on  $\mathcal{T}_o \mathbb{B}^{d,1}$  and  $v$  on  $\mathbb{B}^{d,1}$ , with  $o$  defined on  $\{0, 0_1, \dots, 0_d\} \in \mathbb{B}^{d,1}$ , is shown below:

$$\text{exp}_o^{\mathbb{B},1}(y) = \left( \tanh(\|y\|_2) \frac{y}{\|y\|_2} \right); \text{log}_o^{\mathbb{B},1}(v) = \left( 0, \text{arctanh}(\|v\|_2) \frac{v}{\|v\|_2} \right) \quad (3)$$

We apply projections as described in [40] to constrain points to the manifolds during optimisation. Please refer to appendix 6 for formal definitions of projection.

Next,  $\mathbb{H}^{d,1}$  and  $\mathbb{B}^{d,1}$  are both isomorphic and therefore there exists a diffeomorphism mapping  $\psi$  between  $u \in \mathbb{H}^{d,1}$  and  $v \in \mathbb{B}^{d,1}$  as highlighted below:

$$\psi_{\mathbb{H}^{d,1} \rightarrow \mathbb{B}^{d,1}}(u_0 \dots u_d) = \frac{u_1 \dots u_d}{u_0 + 1}; \quad \psi_{\mathbb{B}^{d,1} \rightarrow \mathbb{H}^{d,1}}(v_1 \dots v_d) = \frac{(1 + \|v\|_2^2, 2v_1 \dots 2v_d)}{1 - \|v\|_2^2} \quad (4)$$

In our work, we apply feature transformations in hyperbolic space, using hyperbolic linear layers [39, 40]. The operations of Mobius addition  $\oplus$  and Mobius scalar multiplication  $\otimes$  in hyperbolic space can be shown to be analogous to the euclidean vector space operations of scalar multiplication and addition. [39] proves that Mobius scalar multiplication is equivalent to applying a logarithmic mapping of point  $v \in \mathbb{B}^{d,1}$  to the tangential space at  $o$  and multiplying the scalar  $r$  before mapping the scaled point back to Poincare space highlighted below:

$$r \otimes v = \text{exp}_o^{\mathbb{B},1}(r \text{log}_o^{\mathbb{B},1}(v)) \quad (5)$$

In a hyperbolic linear layer, we also add a bias term  $b$ . [39] derives a simple equivalent solution to Mobius addition  $(x \oplus b)$  shown in Equation 6. One firstly defines  $b$  on  $\mathcal{T}_o \mathbb{B}^{1,d}$  which is parallel transported to the tangential space  $\mathcal{T}_x \mathbb{B}^{1,d}$  before mapping back to Poincare space. Please refer to appendix 6 for the equations of parallel transport as well as the general form for  $\text{exp}_x^K(y)$  and  $\text{log}_x^K(v)$ .

$$v \oplus b = \text{exp}_v^{\mathbb{B},1}(P_{o \rightarrow v}^1(b)) \quad (6)$$

Equations 5 and 6 can also apply to scalar multiplication and addition in  $\mathbb{H}^{d,1}$  [40]. We now let  $W \in \mathbb{R}^{d' \times d}$  and  $B \in \mathbb{R}^d$  to help define the hyperbolic linear feature transformation  $h(x)$  in  $\mathbb{H}^{d,1}$  and  $\mathbb{B}^{d,1}$  by combining Equations 5 and 6 to form:

$$h(x) = (W \otimes^1 x) \oplus^1 B \quad (7)$$

### 3.1.2 Model discretisation

Let  $\mathcal{D} \subseteq \mathcal{X} \times \mathcal{Y}$  be the dataset, such that elements of  $\mathcal{X}$  are in  $\mathbb{R}^{p \times p}$  and  $\mathcal{Y} = \{1, \dots, N\}$ , where  $p \times p$  and  $N$  correspond to the dimension of an input image and total number of classes, respectively. In this work, we only consider classifiers of the form  $\mathcal{C} = f \circ g$ , where feature extractor  $f : \mathcal{X} \rightarrow \mathcal{E}$  maps input images to the latent space  $\mathcal{E}$  and the feature classifier  $g : \mathcal{E} \rightarrow \mathcal{Y}$  maps the latent space to class labels. We aim to distill the knowledge of a continuous classifier into a hierarchy of related symbols to form an abstraction tree whereby a symbol is a discrete concept represented as a vector. This is based on the valid assumption that the visual world consists of discrete concepts which are related in a hierarchical manner such that abstract visual concepts are the amalgamation of fine-grained discrete features. Therefore, given that the abstraction tree corresponds to an internal representation of the visual world that grows exponentially, this provides the basis to better embed the tree with minimal distortion in hyperbolic  $\mathcal{H}$  rather than Euclidean space  $\mathbb{R}$  [38]. The  $i^{th}$  level in the tree is represented as a hyperbolic codebook  $\zeta^i \in \mathcal{H}^{M_i \times d}$  which provide different levels of abstraction for the continuous space  $\mathcal{E}$ , as shown in Figure 1. The total number of codebooks  $n(\zeta^n)$  and embedding dimensionality  $d$  are hyper-parameters that are selected based on the use case.  $M_0, M_1, \dots, M_n$  are hyper-parameters corresponding to the total number of vectors in codebooks  $\zeta^0, \zeta^1, \dots, \zeta^n$  respectively. The greater  $n$ , the more levels of abstraction and the 'deeper' the explanations. However, we limit  $n$  to an appropriate number to prevent the exponential increase in rules as we strive for an Occam's Razor approach to generate explanations. Given this approach, we carry out ablations to find the smallest  $M_n$  in each codebook to achieve a minimum of 90% knowledge distillation from a pre-trained classifier.

Formally, an abstraction tree is developed by learning the function  $\mathcal{K}$  which collapses the Euclidean continuous latent space  $\mathcal{E}$  into ideally  $\lfloor \log_2 N + 1 \rfloor$  symbols in  $\zeta^n$  as this represents the minimum number of positive symbols to encode  $N$  classes. We can decompose  $\mathcal{K}$  such that  $\mathcal{K} = \mathcal{R} \circ \mathcal{VQ} \circ \mathcal{MD}$ , where  $\mathcal{MD}$  denotes a feature modulation layer before discretisation by vector quantisation ( $\mathcal{VQ}$ ) and  $\mathcal{R}$  expresses the hyperbolic reasoning module.  $\mathcal{R}$  can further be decomposed into  $\mathcal{R}^n \circ \mathcal{R}^{n-1} \circ \dots \circ \mathcal{R}^1$  with the output of each  $\mathcal{R}^l$  computing a different level of abstraction in the form of  $\zeta^i$  (see again Figure 1). We train  $\mathcal{K}$  by sampling  $z$  from  $\mathcal{E}$  and sequentially mapping and discretising  $z$  to increasing levels of abstraction in the abstraction tree to produce  $z_q^i$  with the final level of abstraction used to classify  $z$ .

### 3.1.3 Inductive logic programming

Logic programming is a knowledge representation and reasoning formalism which helps us describe relations of interest in terms of facts and rules expressed in formal logic. Here, rules are usually described in the form of clauses as described in Equation 8, where  $H$  is the *head* of the clause and  $B_1, \dots, B_n$  is the *body* of the clause.

$$H \leftarrow B_1, \dots, B_n \quad (n \geq 1) \quad (8)$$

A clause of this form captures relational information of the form: the head is true when all the elements in the body are true. In this work, we assume that  $H$  and each and every  $B_i$  are atoms, which are Boolean functions amounting to applying predicates to terms (constant or variables).

Inductive Logic Programming (ILP) is a form of logic programming for learning these clauses (as shown in Equation 8) from data. ILP can be formally defined in terms of a tuple  $(\mathcal{B}, \mathcal{P}, \mathcal{N})$ , where  $\mathcal{B}, \mathcal{P}, \mathcal{N}$  correspond to background knowledge, positive and negative examples respectively. The main objective for ILP is to formulate hypotheses (i.e. sets of clauses) given  $\mathcal{B}, \mathcal{P}$ , and  $\mathcal{N}$ . These hypotheses are sets  $\mathcal{C}$  of clauses of the form considered before, such that  $\mathcal{C}$  explains all the examples, formally described as  $\mathcal{B}, \mathcal{C} \models e$  for all positive examples  $e \in \mathcal{P}$  and  $\mathcal{B}, \mathcal{C} \not\models e$  for all negative examples  $e \in \mathcal{N}$ . In general, ILP systems can be built using two main approaches: (i) Bottom-up, starting with analysing  $\mathcal{B}$  to construct a hypothesis that generalises well on  $\mathcal{P}$  and  $\mathcal{N}$ , e.g., Progol [45]; (ii) Top-down approach, where clauses are generated via some pre-defined templates and these clauses are tested for satisfiability on  $\mathcal{P}$  and  $\mathcal{N}$ , e.g., as in Metagol [46] and dILP [47].

TILDE [48] formulates an approach to learn ILP hypotheses via a first-order logical framework for top-down induction of logical decision trees. First order logical decision trees are binary decision trees, where each node corresponds to a conjunction of atoms. In this work, we build on the idea of binary trees to form the component of our hyperbolic reasoning blocks which learns via a bottom-up approach the hierarchical relations/conjunction of atoms in between the codebooks to develop our abstraction tree. We then use this tree to derive hierarchical rules.

### 3.2 Symbol formation

The first step in our framework, symbol formation, initially consists of learning a feature modulation layer ( $\mathcal{MD}$ ) which consists of batch normalisation followed by a  $1 \times 1$  convolutional layer such that  $z_m = \mathcal{MD}(z)$ . This is followed by learning discrete symbols in the form of  $d'$  dimensional vectors using vector quantisation ( $\mathcal{VQ}$ ) to form a fixed sized Euclidean codebook  $\mathbb{C} \in \mathbb{R}^{M_0 \times d'}$  (Figure 1). We do not perform  $\mathcal{VQ}$  in hyperbolic space as we found this significantly less stable.

Given  $(z_q, z_m) \in \mathbb{R}^{K \times d'}$  and  $k \in K$ , we define a deterministic process which maps each embedding vector  $z_{mk} \in z_m$  to the nearest Euclidean codebook vector to form  $z_{qk} \in z_q$  shown below:

$$z_{qk} = \operatorname{argmin}_j \|z_{mk} - \mathbb{C}_j\|_2, \forall k \in K \quad (9)$$

Equation 9 defines a sampling process which is non-differentiable but in order to update/learn the weights of  $\mathcal{MD}$  and the symbols which form  $\mathbb{C}$  based on this sampling method, we apply straight through gradient approximation. This then allows our discrete surrogate model to be trained end to end with the following Quantisation loss [35]:  $\mathcal{L}_{quant} = \|sg(e) - \mathbb{C}\|_2 + \beta \|e - sg(\mathbb{C})\|_2$ . We apply stop gradients (sg) to constrain updates to the appropriate operands [35]. Our ablations determined an optimum value of 0.2 for  $\beta$ . Next, we apply a linear layer with weights  $w_e \in \mathbb{R}^{d \times d'}$  to the Euclidean codebook to reduce the dimensionality to the desired embedding dimensionality  $d$  for  $\zeta^i$  before applying an exponential mapping 3 to Poincare space:  $\zeta^0 \in \mathbb{B}^{M_0 \times d, 1}$ . We choose Poincare space in this work due to the enhanced visual interpretability of 2D embeddings on the Poincare disc [38]. We however note it may be more beneficial for  $\zeta^i$  to be embedded in the hyperboloid when  $d$  is greater than 2 where the advantage of embedding in Poincare space is reduced. We additionally observe improved stability and convergence of  $\zeta^i \in \mathbb{H}^{M_i \times d, 1}$ .

### 3.3 Hyperbolic reasoning module

The second component of our method, the hyperbolic reasoning module ( $\mathcal{R}^l$ ), is similar to the HGCNN [40] but here we learn the edges of the graph (relations/conjunction between  $\zeta^i$  to  $\zeta^{i+1}$ ) using a binary function ( $1 = \text{edge}, 0 = \text{no edge}$ ). This constructs a graph structure equivalent to a tree which is used for reasoning about Euclidean external representations of the visual world. Similar to [40], the first stage of hyperbolic reasoning is a hyperbolic feature transformation shown in Equation 7, which is performed in the unit hyperboloid where we found training to be more stable compared to within the Poincare unit disc/ball. Therefore we map a codebook  $\zeta^i$  from Poincare space to the hyperboloid using Equation 4 before applying a hyperboloid linear layer ( $h(x)^{\mathbb{H}, 1}$ ) to each codebook vector (Equation 7). This is followed by a logarithmic mapping (Equation 2) to  $\mathcal{T}_o\mathbb{H}^{1, d}$ . The second stage of hyperbolic reasoning is the aggregation of symbols in  $\mathcal{T}_o\mathbb{H}^{1, d}$  as proposed in [40] to form  $\zeta^{i+1}$ . This is achieved by first learning the edges or equivalently the property of conjunction over symbols with a binary attention layer [49] in  $\mathcal{R}^l$ , with weights  $w_l^{j, k} \in \mathbb{R}^{j \times k} \in \{0, 1\}, j = 0, 1 \dots M_i, k = 0, 1 \dots M_{i+1}$ . We then perform mean aggregation for the merging of symbols with edges from  $\zeta^i$  to  $\zeta^{i+1}$  by matrix multiplying with weights matrix  $a_l \in \mathbb{R}^{j \times k}$  before mapping back to Poincare space (Equation 3). This aggregation is an approximation of the Freschet mean in hyperbolic space as assumed in [40]. A single pass through  $\mathcal{R}^l$  is summarised in the first line of Equation 10 below with the second line calculating  $a_l^{j, k} \in a_l$ .

$$\begin{aligned} \zeta^{i+1} &= \exp_o^{\mathbb{B}, 1}(a_l^\top \log_o^{\mathbb{H}, 1}(h^{\mathbb{H}, 1}(\psi_{\mathbb{B}^{d, 1} \rightarrow \mathbb{H}^{d, 1}}(\zeta^i)))) \\ a_l^{j, k} &= \begin{cases} \frac{1}{\sum_{j=0}^{M_i} w_l^{j, k}}, & \text{if } w_l^{j, k} = 1 \\ 0, & \text{otherwise} \end{cases} \end{aligned} \quad (10)$$

In order for the hyperbolic reasoning module to update its weights to form an accurate abstraction tree, it needs to classify the discretised samples  $z_q$  from the Euclidean representation,  $\mathcal{E}$ . We firstly

however apply a feature attention function in Euclidean space with continuous weights  $w_l$  constrained between 0 and 1 to learn a reduced linear combination of the features in  $z_q^i$ . This is followed by a mapping to the Poincare unit ball formally defined as  $z_{pq}^i = \text{exp}_{\mathbb{B}^{1,1}}(w_l^\top z_q^i)$  (see Equation 3). Next, every  $z_{pqk'}^i \in z_{pq}^i$  is mapped to the nearest codebook vector by Poincare distance in  $\zeta^i$  using Equation 1 to form  $z_{pq}^{i+1}$ . Note, unlike in  $\mathcal{VQ}$  for symbol formation, we do not directly update the symbols in  $\zeta_i$  so that it is only learned by a function  $R^l$  of  $\zeta_{i-1}$  in order to faithfully learn an abstraction tree. Therefore, straight through gradient approximation is not required in this abstraction process. We complete abstraction by moving our discrete sample back into Euclidean space to form  $z_q^{i+1}$  by computing  $\text{log}_o^{\mathbb{B}^{1,1}}(z_{pq}^{i+1})$  (Equation 3). The feature attention function is necessary due to there being multiple edges from a single child symbol. Feature attention ensures the most likely symbol is sampled by being aware of the neighbouring symbols in  $z_q^i$  which prevents the hierarchy from collapsing into one single discrete symbol. For example, in Figure 2,  $\zeta_2^0$  is related to  $\zeta_1^1$  and  $\zeta_2^1$ ; therefore assuming  $z_q^i$  containing  $\zeta_2^0$  also has  $\zeta_1^0$  but not  $\zeta_3^0$ , then  $\zeta_2^0$  maps to  $\zeta_1^1$  as  $\zeta_1^0$  is related to  $\zeta_1^1$ .

Finally,  $z_q^n$  is mapped to the class prediction by average pooling to a linear class projection layer (Figure 1) to match the dimensionality of the output. The knowledge distillation loss is defined as the cross-entropy loss between the classifiers prediction ( $y$ ) and the hyperbolic discrete surrogate model’s prediction ( $\hat{y}$ ):  $\mathcal{L}_{dist}(\hat{y}, y)$ . We determine that the Poincare distances (Equation 1) between codebooks correspond to graph distances in the tree. Therefore a Poincare codebook loss  $\mathcal{L}_{Poincare}$  is calculated such that symbols with an edge are closer together and those without an edge are pushed apart in hyperbolic space. First, let  $u$  to be any codebook vector in the set of all  $\zeta^{i\dots n}$  while  $v$  and  $v'$  are defined as codebook vectors with and without an edge with  $u$  respectively, then two sets  $\mathcal{P}$  and  $\mathcal{W}$  are created such that;  $u, v \in \mathcal{P}$  and  $u, v' \in \mathcal{W}$ . Given this, we can express the Poincare codebook loss as follows:  $\mathcal{L}_{Poincare} = \frac{\sum_{u,v \in \mathcal{P}} e^{d^{\mathbb{B}^{1,1}}(u,v)}}{\sum_{u,v' \in \mathcal{W}} e^{d^{\mathbb{B}^{1,1}}(u,v' )}}$ . We now define our total training loss as:  $\mathcal{L}_{Total} = \mathcal{L}_{dist} + \mathcal{L}_{quant} + \mathcal{L}_{Poincare}$ .

All continuous weights in our model framework are updated with Adam optimisation while the binary weights in  $\mathcal{R}^l$  are updated using the *Bop* algorithm proposed by [49]. In this algorithm, the strength of gradient signal at time  $t$  is determined by looking at the continuous exponential moving average  $m_t$  of accumulated gradients up to the gradient,  $g_t$  at  $t$ . The binary weights are then updated subjected to  $m_t$  exceeding a threshold  $\tau$  and the sign of  $w_{t,l}^{j,k}$  matching  $m_t$ . In our case, we map our weights to  $\{0, 1\}$  rather than  $\{-1, 1\}$ , by initializing weights randomly  $\in \{0, 1\}$  and modify the update rule proposed in [49]. This is shown in Equation 11 below, where the first line corresponds to gradient strength where  $\gamma$  is the adaptivity rate [49] and the second line defines the update rule [49]. Please refer to appendix 6 for further training details.

$$m_t = (1 - \gamma)m_{t-1} + \gamma g_t$$

$$w_{t,l}^{j,k} = \begin{cases} |w_{t-1,l}^{j,k} - 1|, & \text{if } |m_t^i| > \tau \text{ and } \text{sign}(m_t^i) = \text{sign}(w_{t-1,l}^{j,k}) \\ w_{t-1,l}^{j,k}, & \text{otherwise} \end{cases} \quad (11)$$

### 3.4 Explanations and visual semantics

We now aim to generate a hierarchy of rules explaining the reasons behind the classifier’s decision. At the end of training, all codebook symbols without an edge to or from itself are dropped and an abstraction tree is constructed based on the edges learnt between codebooks. We provide both global class-level and local example-level induced abstraction trees as a part of our explanation, along with the visual semantics for symbols in the example-level tree.

In Figure 2, we have two codebooks  $\zeta^0$  and  $\zeta^1$  each with 4 and 3 symbols, which are getting abstracted to form the concept;  $Class_0$  and  $Class_1$ . A class-level induced tree indicates the subtree corresponding to a specific class. For example, in 2, the subtree for  $Class_0$  consists of symbols,  $\zeta_0^0, \zeta_2^0, \zeta_1^1$  and  $Class_0$ . An image level tree is input dependent, and forms a subtree of a class-level tree.

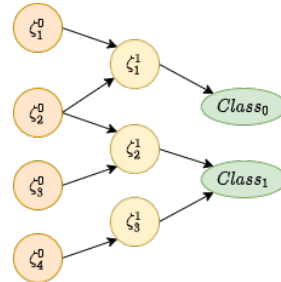


Figure 2: Example abstraction tree

The extraction of visual rules, first requires us to train a decoder block to reconstruct images in Euclidean space as perceived by the classifier, with a reconstruction loss  $\mathcal{L}_{recon} = \|\mathbb{D}(z_q) - x\|_2^2$ , where  $z_q \sim \mathbb{C}$  and  $x \sim \mathcal{X}$  described in figure 1. During training, we make sure that the gradients from the decoder block do not affect the weights of the discrete surrogate model, to maintain faithfulness of the discretisation process. In order to explain the semantic meaning of any symbol;  $\zeta_j^i \in z_q^i$ , we must project the selected symbol onto  $\mathbb{C}$  and visualise the semantic difference using a decoder  $\mathbb{D}$ . In the first step to compute the semantic difference  $\delta(\hat{x})$ , we deduce all the symbols in  $z_q^0 \sim \zeta^0$  responsible for activating  $\zeta_j^i \in z_q^i$  using the image-level tree to form a set  $\mathcal{S} \subset z_q^0$ .  $\zeta^0$  has a one to one mapping with  $\mathbb{C}$  such that one can now form a new set  $\mathcal{A} \subset z_q$ . We use  $\mathcal{A}$  to perform a controlled intervention on  $z_q \sim \mathbb{C}$  which is inputted into  $\mathbb{D}$  to calculate  $\delta(\hat{x})$ . We can formally define this process as:  $\delta(\hat{x}) = \mathbb{D}(z_q) - \mathbb{D}(z_q; do(z_{qk} = 0), \forall z_{qk} \in \mathcal{A})$ , where  $z_{qk} \in z_q$ .

## 4 Experiments

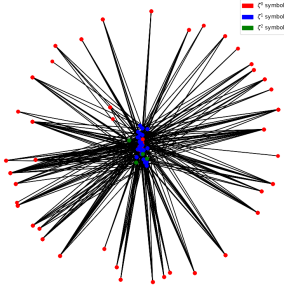


Figure 3: 2D Poincare embedding of symbols obtained for MNIST. Red, blue, and green nodes indicate symbols from  $\zeta^0, \zeta^1, \zeta^2$  respectively

We use our framework to explain two pre-trained classifiers, one trained on the MNIST dataset [50] as a proof of concept study and the other trained on the AFHQ dataset [51] to indicate the scalability and generalisability of our proposed method. In the following experiments, we choose a 3 level hierarchy. We determine through our ablations, the number of codebook vectors for each level  $M_i$ , to be 128, 32, and 4 for the MNIST experiment and 256, 64, and 2 for AFHQ. Please refer to appendix 6 for information on classifier models and codebook ablations.

We hypothesise that hyperbolic embeddings will better embed a hierarchical tree without distortion and hence allow to reduce the dimensionality  $d$  of  $\zeta^i$  such that knowledge distillation would not be affected. We support this hypothesis by achieving better knowledge distillation accuracy with Poincare embeddings highlighted in table 1. One also notes increasingly better performance as we reduce the dimensionality of  $\zeta^i$  down to 2 on the MNIST and AFHQ dataset. Figure 3 shows the 2 dimensional embeddings on the Poincare disk for the MNIST dataset maintaining a robust hierarchy.

Next, we qualitatively compare the explanations obtained from our framework against standard explainability frameworks: LIME [8], DeepSHAP [9], deepLIFT [10], and gradCAM [11]. Figure 4 describes the explanations obtained from standard existing methods. It is clear that most of the existing explanation methods focus on either pixel importance or gradient-based attention and do not differentiate the effect of multiple concepts. These explanations also are quite limited without yielding any sort of reasoning.

Our proposed method go beyond feature attribution by allowing the user to decide on the level of abstractness upon which to provide the symbolic and corresponding visual semantic rules which make up explanations. Figure 5 demonstrates the effectiveness of our explanations on a pre-trained classifier for MNIST. Figure 5(a) shows the class-level *global-tree* representing our trained reasoning blocks; this tree includes all possible symbol abstractions for a particular class. To explain a given image we construct a image-level *local-tree* which is described in Figure 5(b). Figure 5(c) provides a visual description of an image-level tree where we plot a single visual rule from each abstract level of reasoning. In this example, the visual semantics for a rule obtained for a given image  $x$  corresponding to  $\text{Class6}(x) \leftarrow \zeta_5^2(x), \zeta_1^2(x)$  is described in the first row of Figure 5(c). The second row of Figure 5(c) visualises the obtained rule corresponding to  $\zeta_1^2(x) \leftarrow \zeta_3^1(x), \zeta_{25}^1(x)$  while the last row visualises how  $\zeta_{25}^1$  is obtained using symbols from  $\zeta^0$ . As we go down the level of abstraction or in other terms, as we move closer to the boundary of Poincare space 3, visually the symbols start to move from

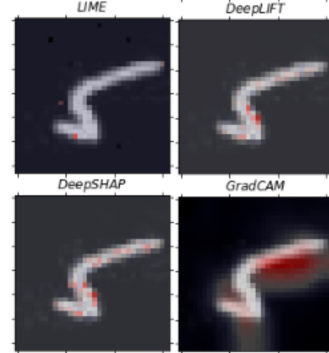


Figure 4: Illustration of existing explanation techniques, top-left, top-right, bottom-left, and bottom-right corresponds to LIME, DeepLIFT, DeepSHAP, and GradCAM explanations respectively.



a complete digit heatmap to a more focused region in a digit, demonstrating a visual hierarchical explanation. One can also note the distinct semantic differences between individual symbols highlighting the advantage of discretising features. Similar explanations and visual semantic behaviour can be observed for a model trained on the AFHQ dataset shown in Figure 12 where we again observe symbols getting localized as we go deeper into the hierarchy. Please refer to appendix 6 for further details and examples.

Table 1: Knowledge distillation accuracy of different dimensional Euclidean and Poincare embeddings on the MNIST and AFHQ classifiers.

Embedding dim → Dataset ↓	Poincare			Euclidean		
	2	4	16	2	4	16
MNIST	<b>0.90</b>	<b>0.96</b>	<b>0.99</b>	0.81	0.92	0.95
AFHQ	<b>0.90</b>	<b>0.95</b>	<b>0.98</b>	0.80	0.90	0.97

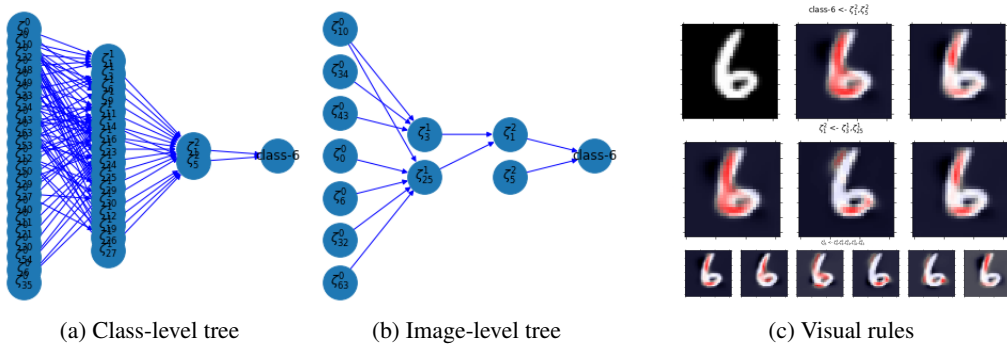


Figure 5: This figure describes the explanations obtained using the proposed framework for a MNIST classifier.  $\zeta^i \in \mathbb{B}^{M_i \times 16, 1}$  (a) Demonstrates the obtained class-level tree, which is a complete set of symbols responsible for entailing class; '6', (b) indicates a image-level tree with symbols responsible for making a decision for a given image, and (c) demonstrates the some of the visual rules obtained from a image-level tree.

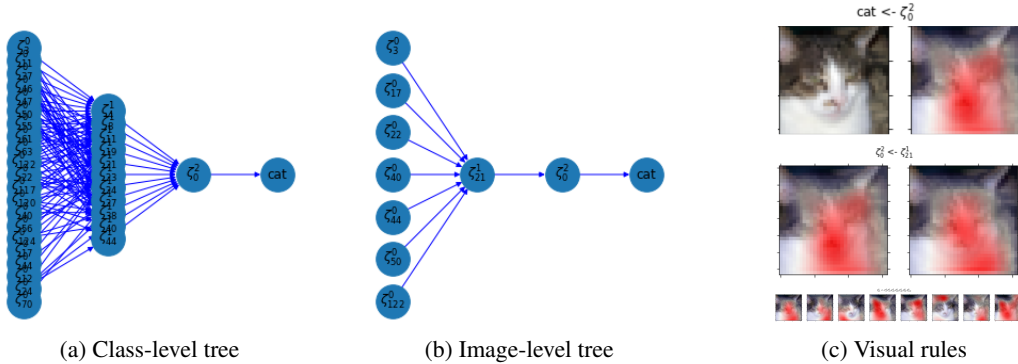


Figure 6: This figure describes the explanations obtained using the proposed framework for a AFHQ classifier for the class; 'cat'.  $\zeta^i \in \mathbb{B}^{M_i \times 16, 1}$

## 5 Conclusion

This work provides novel hierarchical explanations for deep discriminative models, which was demonstrated on the MNIST and AFHQ datasets. The proposed framework discretises the continuous latent space of classifiers into  $M_0$  discrete features, followed by multiple layers of reasoning and discrete abstraction in hyperbolic space to form an abstraction tree which provide hierarchical rules as explanations for the Euclidean visual world. We demonstrate hyperbolic geometry allows to embed our knowledge tree with minimal distortion compared to the Euclidean counterpart. The results show

the existence of consistent and distinct symbolic hierarchical rules for each class which is visualised by generating attention regions in an image. For future work, our framework can be developed into a stand-alone deep discriminative neuro-symbolic model which improves generalisability as well as interpretability. We can here also explore the advantage of learnable curvature similar to [40] to embed symbolic data in hyperbolic space. We plan to extend this method with domain experts to assign semantic meaning to symbols and extract high-level descriptive explanations as well as highlight biases and inconsistencies in features learned by a given model.

**Acknowledgements.** This work was supported and funded by Cancer Research UK (CRUK) (C309/A28804) and UKRI centre for Doctoral Training in Safe and Trusted AI (EP/S023356/1).

## References

- [1] Finale Doshi-Velez, Ryan Budish, and Mason Kortz. The role of explanation in algorithmic trust. Technical report, Technical report, Artificial Intelligence and Interpretability Working Group . . . , 2017.
- [2] Joshua Alexander Kroll. *Accountable algorithms*. PhD thesis, Princeton University, 2015.
- [3] Been Kim, Martin Wattenberg, Justin Gilmer, Carrie Cai, James Wexler, Fernanda Viegas, et al. Interpretability beyond feature attribution: Quantitative testing with concept activation vectors (tcav). In *International conference on machine learning*, pages 2668–2677. PMLR, 2018.
- [4] Zachary C Lipton. The mythos of model interpretability: In machine learning, the concept of interpretability is both important and slippery. *Queue*, 16(3):31–57, 2018.
- [5] Wolfgang Stammer, Patrick Schramowski, and Kristian Kersting. Right for the right concept: Revising neuro-symbolic concepts by interacting with their explanations. In *Proceedings of the IEEE/CVF Conference on Computer Vision and Pattern Recognition*, pages 3619–3629, 2021.
- [6] Andrew K Lampinen, Nicholas A Roy, Ishita Dasgupta, Stephanie CY Chan, Allison C Tam, James L McClelland, Chen Yan, Adam Santoro, Neil C Rabinowitz, Jane X Wang, et al. Tell me why!—explanations support learning of relational and causal structure. *arXiv preprint arXiv:2112.03753*, 2021.
- [7] Geoffrey Irving, Paul Christiano, and Dario Amodei. Ai safety via debate. *arXiv preprint arXiv:1805.00899*, 2018.
- [8] Marco Tulio Ribeiro, Sameer Singh, and Carlos Guestrin. " why should i trust you?" explaining the predictions of any classifier. In *Proceedings of the 22nd ACM SIGKDD international conference on knowledge discovery and data mining*, pages 1135–1144, 2016.
- [9] Scott M Lundberg and Su-In Lee. A unified approach to interpreting model predictions. In I. Guyon, U. V. Luxburg, S. Bengio, H. Wallach, R. Fergus, S. Vishwanathan, and R. Garnett, editors, *Advances in Neural Information Processing Systems*, volume 30. Curran Associates, Inc., 2017.
- [10] Avanti Shrikumar, Peyton Greenside, and Anshul Kundaje. Learning important features through propagating activation differences. In *International conference on machine learning*, pages 3145–3153. PMLR, 2017.
- [11] Ramprasaath R Selvaraju, Michael Cogswell, Abhishek Das, Ramakrishna Vedantam, Devi Parikh, and Dhruv Batra. Grad-cam: Visual explanations from deep networks via gradient-based localization. In *Proceedings of the IEEE international conference on computer vision*, pages 618–626, 2017.
- [12] Aditya Chattopadhyay, Anirban Sarkar, Prantik Howlader, and Vineeth N Balasubramanian. Grad-cam++: Generalized gradient-based visual explanations for deep convolutional networks. In *2018 IEEE winter conference on applications of computer vision (WACV)*, pages 839–847. IEEE, 2018.
- [13] Sam Sattarzadeh, Mahesh Sudhakar, Konstantinos N Plataniotis, Jongseong Jang, Yeonjeong Jeong, and Hyunwoo Kim. Integrated grad-cam: Sensitivity-aware visual explanation of deep convolutional networks via integrated gradient-based scoring. In *ICASSP 2021-2021 IEEE International Conference on Acoustics, Speech and Signal Processing (ICASSP)*, pages 1775–1779. IEEE, 2021.

- [14] Yash Goyal, Ziyang Wu, Jan Ernst, Dhruv Batra, Devi Parikh, and Stefan Lee. Counterfactual visual explanations. In *International Conference on Machine Learning*, pages 2376–2384. PMLR, 2019.
- [15] Amirata Ghorbani, James Wexler, James Zou, and Been Kim. Towards automatic concept-based explanations. *arXiv preprint arXiv:1902.03129*, 2019.
- [16] Asma Ghandeharioun, Been Kim, Chun-Liang Li, Brendan Jou, Brian Eoff, and Rosalind W Picard. Dissect: Disentangled simultaneous explanations via concept traversals. *arXiv preprint arXiv:2105.15164*, 2021.
- [17] Avinash Kori, Parth Natekar, Balaji Srinivasan, and Ganapathy Krishnamurthi. Interpreting deep neural networks for medical imaging using concept graphs. In *International Workshop on Health Intelligence*, pages 201–216. Springer, 2021.
- [18] Axel Sauer and Andreas Geiger. Counterfactual generative networks. *arXiv preprint arXiv:2101.06046*, 2021.
- [19] Chun-Hao Chang, Elliot Creager, Anna Goldenberg, and David Duvenaud. Explaining image classifiers by counterfactual generation. *arXiv preprint arXiv:1807.08024*, 2018.
- [20] Daniel Nemirovsky, Nicolas Thiebaut, Ye Xu, and Abhishek Gupta. CounterGAN: Generating realistic counterfactuals with residual generative adversarial nets. *arXiv preprint arXiv:2009.05199*, 2020.
- [21] Oran Lang, Yossi Gandelsman, Michal Yarom, Yoav Wald, Gal Elidan, Avinatan Hassidim, William T Freeman, Phillip Isola, Amir Globerson, Michal Irani, et al. Explaining in style: Training a gan to explain a classifier in stylespace. *arXiv preprint arXiv:2104.13369*, 2021.
- [22] Sharon Lee Armstrong, Lila R Gleitman, and Henry Gleitman. What some concepts might not be. *Cognition*, 13(3):263–308, 1983.
- [23] Daniel C Burnston and Philipp Haueis. Evolving concepts of “hierarchy” in systems neuroscience. In *Neural Mechanisms*, pages 113–141. Springer, 2021.
- [24] Drew Hudson and Christopher D Manning. Learning by abstraction: The neural state machine. *Advances in Neural Information Processing Systems*, 32, 2019.
- [25] Ramakrishna Vedantam, Karan Desai, Stefan Lee, Marcus Rohrbach, Dhruv Batra, and Devi Parikh. Probabilistic neural symbolic models for interpretable visual question answering. In *International Conference on Machine Learning*, pages 6428–6437. PMLR, 2019.
- [26] Jiayuan Mao, Chuang Gan, Pushmeet Kohli, Joshua B Tenenbaum, and Jiajun Wu. The neuro-symbolic concept learner: Interpreting scenes, words, and sentences from natural supervision. *arXiv preprint arXiv:1904.12584*, 2019.
- [27] Kexin Yi, Jiajun Wu, Chuang Gan, Antonio Torralba, Pushmeet Kohli, and Josh Tenenbaum. Neural-symbolic vqa: Disentangling reasoning from vision and language understanding. *Advances in neural information processing systems*, 31, 2018.
- [28] James Tee and Desmond P Taylor. Is information in the brain represented in continuous or discrete form? *IEEE Transactions on Molecular, Biological and Multi-Scale Communications*, 6(3):199–209, 2020.
- [29] Petra Vetter and Albert Newen. Varieties of cognitive penetration in visual perception. *Consciousness and cognition*, 27:62–75, 2014.
- [30] CM Wessinger, J VanMeter, Biao Tian, J Van Lare, James Pekar, and Josef P Rauschecker. Hierarchical organization of the human auditory cortex revealed by functional magnetic resonance imaging. *Journal of cognitive neuroscience*, 13(1):1–7, 2001.
- [31] David Meunier, Renaud Lambiotte, Alex Fornito, Karen Ersche, and Edward T Bullmore. Hierarchical modularity in human brain functional networks. *Frontiers in neuroinformatics*, 3:37, 2009.
- [32] Claire Glanois, Xuening Feng, Zhaohui Jiang, Paul Weng, Matthieu Zimmer, Dong Li, and Wulong Liu. Neuro-symbolic hierarchical rule induction. *arXiv preprint arXiv:2112.13418*, 2021.
- [33] Ludovico Mitchener, David Tuckey, Matthew Crosby, and Alessandra Russo. Detect, understand, act: A neuro-symbolic hierarchical reinforcement learning framework. *Machine Learning*, pages 1–27, 2022.

- [34] Rita Sharma and David Poole. Probabilistic reasoning with hierarchically structured variables. In *IJCAI*, pages 1391–1397. Citeseer, 2005.
- [35] Aaron Van Den Oord, Oriol Vinyals, et al. Neural discrete representation learning. *Advances in neural information processing systems*, 30, 2017.
- [36] Maximilian Nickel, Xueyan Jiang, and Volker Tresp. Reducing the rank in relational factorization models by including observable patterns. *Advances in Neural Information Processing Systems*, 27, 2014.
- [37] Frederic Sala, Chris De Sa, Albert Gu, and Christopher Ré. Representation tradeoffs for hyperbolic embeddings. In *International conference on machine learning*, pages 4460–4469. PMLR, 2018.
- [38] Maximilian Nickel and Douwe Kiela. Poincaré embeddings for learning hierarchical representations. *Advances in neural information processing systems*, 30, 2017.
- [39] Octavian Ganea, Gary Bécigneul, and Thomas Hofmann. Hyperbolic neural networks. *Advances in neural information processing systems*, 31, 2018.
- [40] Ines Chami, Zhitao Ying, Christopher Ré, and Jure Leskovec. Hyperbolic graph convolutional neural networks. *Advances in neural information processing systems*, 32, 2019.
- [41] Qi Liu, Maximilian Nickel, and Douwe Kiela. Hyperbolic graph neural networks. *Advances in Neural Information Processing Systems*, 32, 2019.
- [42] Stephen Muggleton, Wang-Zhou Dai, Claude Sammut, Alireza Tamaddoni-Nezhad, Jing Wen, and Zhi-Hua Zhou. Meta-interpretive learning from noisy images. *Machine Learning*, 107(7):1097–1118, 2018.
- [43] Dianhuan Lin, Eyal Dechter, Kevin Ellis, Joshua B Tenenbaum, and Stephen H Muggleton. Bias reformulation for one-shot function induction. 2014.
- [44] Donald Michie. Machine learning in the next five years. In *Proceedings of the 3rd European conference on European working session on learning*, pages 107–122, 1988.
- [45] Stephen Muggleton. Inverse entailment and prolog. *New generation computing*, 13(3):245–286, 1995.
- [46] Andrew Cropper and Stephen H. Muggleton. Metagol system. <https://github.com/metagol/metagol>, 2016.
- [47] Richard Evans and Edward Grefenstette. Learning explanatory rules from noisy data. *Journal of Artificial Intelligence Research*, 61:1–64, 2018.
- [48] Hendrik Blockeel and Luc De Raedt. Top-down induction of first-order logical decision trees. *Artificial intelligence*, 101(1-2):285–297, 1998.
- [49] Koen Helwegen, James Widdicombe, Lukas Geiger, Zechun Liu, Kwang-Ting Cheng, and Roeland Nusselder. Latent weights do not exist: Rethinking binarized neural network optimization. *Advances in neural information processing systems*, 32, 2019.
- [50] Li Deng. The mnist database of handwritten digit images for machine learning research [best of the web]. *IEEE signal processing magazine*, 29(6):141–142, 2012.
- [51] Yunjeong Choi, Youngjung Uh, Jaejun Yoo, and Jung-Woo Ha. Stargan v2: Diverse image synthesis for multiple domains. In *Proceedings of the IEEE/CVF conference on computer vision and pattern recognition*, pages 8188–8197, 2020.
- [52] Hongyi Zhang, Sashank J Reddi, and Suvrit Sra. Riemannian svrg: Fast stochastic optimization on riemannian manifolds. *Advances in Neural Information Processing Systems*, 29, 2016.
- [53] Kaiming He, Xiangyu Zhang, Shaoqing Ren, and Jian Sun. Identity mappings in deep residual networks. In *European conference on computer vision*, pages 630–645. Springer, 2016.
- [54] Forrest Iandola, Matt Moskewicz, Sergey Karayev, Ross Girshick, Trevor Darrell, and Kurt Keutzer. Densenet: Implementing efficient convnet descriptor pyramids. *arXiv preprint arXiv:1404.1869*, 2014.

## 6 Appendix

### 6.1 Hyperbolic mappings

We show here the general equations  $exp_x^K(y)$  and  $log_x^K(v)$  with any negative curvature,  $-1/K$  for  $\mathbb{H}^{d,K}$  in Equation 12 and 13 respectively as well as for  $\mathbb{B}^{d,K}$  in Equation 14 and 15 respectively [40, 39].

#### 6.1.1 Hyperboloid

$$exp_x^{\mathbb{H},K}(y) = \cosh\left(\frac{\|y\|_S}{\sqrt{K}}\right) x + \sqrt{K} \sinh\left(\frac{\|y\|_S}{\sqrt{K}}\right) \frac{y}{\|y\|_S} \quad (12)$$

$$log_x^{\mathbb{H},K}(v) = d^{\mathbb{H},K}(x, v) \left( \frac{v + \frac{1}{K} \langle x, v \rangle_S x}{\|v + \frac{1}{K} \langle x, v \rangle_S x\|_S} \right) \quad (13)$$

#### 6.1.2 Poincare

A Riemannian metric tensor is conformal to another Riemannian metric if it defines the same angles. In the case of the Poincare unit ball, there is a smooth conformal mapping,  $\lambda : \mathbb{B} \rightarrow \mathbb{R}$  between the Euclidean metric tensor  $g_x^{\mathbb{R}}$  and Poincare metric tensor  $g_x^{\mathbb{B},1}$ . The Poincare conformal factor  $\lambda_x = \frac{2}{1-\|x\|^2}$  is defined such that  $g_x^{\mathbb{B},1} = \lambda_x^2 g_x^{\mathbb{R}}$ .

$$exp_x^{\mathbb{B},K}(y) = x \oplus^K \left( \tanh\left(\frac{\sqrt{K} \lambda_x^K \|y\|}{2}\right) \frac{y}{\sqrt{K} \|y\|} \right) \quad (14)$$

$$log_x^{\mathbb{B},K}(v) = \frac{2}{\sqrt{K} \lambda_x^K} \operatorname{arctanh}(\sqrt{K} \|-x \oplus^K v\|) \frac{-x \oplus^K v}{\|-x \oplus^K v\|} \quad (15)$$

### 6.2 Parallel transport

In this section, we reveal the equations of parallel transport for vector  $b$  on the tangential space of the origin to the tangential space of  $v$ . Formally, we show  $P_{o \rightarrow v}^K(b)$  in  $\mathbb{B}^{K,d}$  and  $\mathbb{H}^{K,d}$  below.

#### 6.2.1 Hyperboloid

The general form of this equation,  $P_{x \rightarrow v}^K(b)$  shown below in Equation 16 is derived in [40].

$$P_{o \rightarrow v}^K(b) = b - \frac{\langle log_o(v), b \rangle_S}{d^{\mathbb{H},1}(o, v)^2} (log_o(v) + log_v(o)) \quad (16)$$

#### 6.2.2 Poincare

Equation 17 is derived in [39].

$$P_{o \rightarrow v}^K(b) = \frac{\lambda_o^K}{\lambda_v^K} b \quad (17)$$

### 6.3 Projections

We need to apply projections to constrain points to the manifolds and its tangential space after optimising. In our work, all operations are performed in the tangential plane and therefore one needs to only apply projections after the exponential mapping from the tangential space to the manifold which we define below.

Equation 18, below shows the projection after exponential mapping  $y$  on  $\mathcal{T}_x \mathbb{H}^{d,K}$  to the hyperboloid manifold  $\mathbb{H}^{d,K}$ . In our work we use  $K = 1$  for applying projections.

$$Proj(exp_x^{\mathbb{H},K}(y)) = (\sqrt{1 + \|v_{1:d}\|_2^2}, v_{1:d}) \quad (18)$$

The projection when mapping a point  $y$  on  $\mathcal{T}_x \mathbb{B}^{d,K}$  to Poincare space  $\mathbb{B}^{d,K}$  is achieved by normalising  $exp_x^{\mathbb{B},K}(y)$  if  $\|exp_x^{\mathbb{B},K}(y)\|_2^2 > 1/\sqrt{K}$  or  $> 1$  in the case of the Poincare unit ball.

## 6.4 Training details and architectures

### 6.4.1 Discrete surrogate model

We consider an image dimension of  $32 \times 32$  and  $64 \times 64$  for the MNIST and AFHQ dataset respectively. Our modulation layer reduces the number features (latent dimension) of  $z$  from 64 to 8 channels and 1024 to 32 channels for the MNIST and AFHQ experiments respectively. We perform all hyperbolic linear operations in  $\mathcal{T}_x\mathbb{H}$  and do not directly update the embeddings  $\zeta^i \in \mathbb{H}^{1,d}$  or  $\in \mathbb{B}^{1,d}$  which means we can perform Euclidean optimisation. Therefore, for the experiments in the main paper, we use Adam optimisation with a learning rate of 0.0002 and batch size of 50 in all experiments to train the discrete surrogate model for 40 epochs. We experimented with Riemmanian stochastic gradient descent [52] but found Adam optimisation to be more stable. We also found that  $\zeta^n \in \mathbb{H}^{M_i \times d, 1}$  provided greater stability during training and showed generally improved performance (see codebook ablation tables 2 and 3 below in section 6.5)

We described the optimisation of the Binary weights in the main paper. In our experiments, we use, adaptivity rate  $\gamma$  of 0.0004 and threshold  $\tau$  of  $1e - 8$ . The adaptivity rate is analogous to the learning rate and can be seen as the consistency of a gradient signal required to induce a flip in weights from 0 to 1 or vice versa [49]. A high  $\gamma$  can therefore induce a flip quicker given a new gradient signal but this can also mean noisy training [49].  $\tau$  is reflective of the strength of the gradient signal required to induce a flip [49].

### 6.4.2 Decoder

The Decoder for MNIST experiments initially consists of a  $1 \times 1$  convolutional block to increase the number of channels back to 64 channels before 3 up-sampling blocks. Each up-sampling block consists of bi-linear interpolation before two pre-activation  $3 \times 3$  convolutional blocks with residual connections [53]. We use batch normalisation and ReLU activation. In our AFHQ experiments, the decoder also initially starts with a  $1 \times 1$  convolutional block to increase the number of channels back to 1024 before 4 up-sampling blocks identical to the one used in our MNIST experiments. We train the decoder in both experiments for 40 epochs using Adam optimisation with a learning rate of 0.0002.

### 6.4.3 Pre-trained classifiers

The MNIST pre-trained classifier consists of 7 convolutional blocks made up of a  $3 \times 3$  convolutional layer followed by batch normalisation and ReLU non-linearity. This is followed by global average pooling and a single layer linear classifier. Max pooling is applied after the first, third and fifth layers. The number of channels corresponding to the final convolutional block is 64. We train this classifier for 50 epochs with a batch size of 50. We use Adam optimisation with an initial learning rate of 0.01 and weight decay of 0.01. We achieve 99% accuracy with this pre-trained classifier

We use the DenseNet-121 as our pre-trained classifier for the AFHQ dataset [54]. We train using Adam optimisation with an initial learning rate of 0.001 and weight decay of 0.05. 98% accuracy is achieved with this classifier. We reduce the dimensionality of the MNIST and AFHQ images to  $4 \times 4$  in the final layer before being inputted into the classifier.

### 6.4.4 Optional commitment loss

Given  $z_{pq}^i \in \mathbb{R}^{K \times d'}$  and  $k \in K$ , we define an optional commitment loss to move each  $z_{pqk}^i \in z_{pq}^i$  closer to its sampled codebook vector denoted  $\zeta_k^i$  shown below in Equation 19.

$$\mathcal{L}_{cb} = \sum_{i=0}^{i=n} \sum_{t=0}^{t=K} d^{\mathbb{B},1}(z_{pqk}^i, sg(\zeta_k^i)). \quad (19)$$

Therefore the total loss in this case is:  $\mathcal{L}_{Total} = \mathcal{L}_{dist} + \mathcal{L}_{quant} + \mathcal{L}_{Poincare} + \epsilon \mathcal{L}_{cb}$ ,  $\epsilon \in \{0, 1\}$ .

We found this to not affect knowledge distillation performance except to provide a more committed notion of abstraction for  $z_q^i$

## 6.5 Codebook ablations

We run multiple codebook ablations to find the minimum number of codebook vectors required to achieve a knowledge distillation accuracy of at least 90% shown in table 2 and 3. We fix the number of codebook vectors in  $\zeta^n$  to  $\lfloor \log_2 N + 1 \rfloor$ . We note in more complex datasets, a larger number of codebook vectors maybe required in  $\zeta^n$ , whereby a class may need to be encoded with more than one possible combination of codebook vectors in order to fit the data. We also compare knowledge distillation accuracy of codebooks with Poincare embeddings against hyperboloid embeddings. In these experiments we only use a three level hierarchy. The user can however decide if they would like more levels of abstraction by increasing the number of codebooks. We note also, the use of codebook ablations is a limitation for the practicality of our explainability method.

Table 2: Knowledge distillation accuracy of different codebook sizes for Poincare, Hyperboloid and Euclidean embeddings on the MNIST dataset. The best knowledge distillation accuracy for each embedding dimension is highlighted in bold.

Embedding dim. ( $\rightarrow$ ) Codebook Size ( $\zeta^0, \zeta^1, \zeta^2$ ) ( $\downarrow$ )	Poincare			Hyperboloid			Euclidean		
	2	4	16	2	4	16	2	4	16
512, 64, 4	0.92	0.91	0.98	<b>0.95</b>	<b>0.93</b>	<b>0.99</b>	0.80	0.90	0.95
256, 64, 4	<b>0.94</b>	0.94	<b>0.99</b>	0.91	<b>0.98</b>	<b>0.99</b>	0.86	0.92	0.96
256, 32, 4	0.89	0.96	<b>0.99</b>	<b>0.93</b>	<b>0.98</b>	0.97	0.79	0.91	0.98
128, 32, 4	0.90	<b>0.96</b>	<b>0.99</b>	<b>0.91</b>	0.95	<b>0.99</b>	0.81	0.92	0.95
64, 16, 4	0.85	<b>0.88</b>	<b>0.94</b>	<b>0.90</b>	<b>0.88</b>	0.93	0.80	0.83	0.90

Table 3: Knowledge distillation accuracy of different codebook sizes for Poincare, Hyperboloid and Euclidean embeddings on the AFHQ dataset. The best knowledge distillation accuracy for each embedding dimension is highlighted in bold.

Embedding dim. ( $\rightarrow$ ) Codebook Size ( $\zeta^0, \zeta^1, \zeta^2$ ) ( $\downarrow$ )	Poincare			Hyperboloid			Euclidean		
	2	4	16	2	4	16	2	4	16
512, 64, 2	<b>0.94</b>	0.92	0.96	0.90	<b>0.95</b>	<b>0.98</b>	0.83	0.91	0.93
256, 64, 2	0.90	0.95	0.98	<b>0.92</b>	<b>0.98</b>	<b>0.99</b>	0.80	0.90	0.97
256, 32, 2	0.86	0.85	0.93	<b>0.88</b>	<b>0.91</b>	<b>0.96</b>	0.77	0.81	0.88
128, 32, 2	<b>0.88</b>	0.88	0.91	0.84	<b>0.92</b>	<b>0.96</b>	0.80	0.86	0.90
64, 16, 2	0.78	0.85	0.83	<b>0.81</b>	<b>0.90</b>	<b>0.92</b>	0.75	0.80	0.84

## 6.6 Additional results

In this section, we provide additional examples illustrating the explanations of the proposed framework. Figure 7 and 8 describes our explanations for a model trained on the MNIST dataset classifying class '3', and '9' respectively. Figure 12 and 11 describes our explanations for a model trained on the AFHQ dataset classifying class 'dog' and 'cat' respectively. The sub-figure (a) in Figure 7, 8, 12, and 11 demonstrates the local image-level abstraction tree reflecting how definite symbols from codebook  $\zeta^0$  combine to form abstract symbols in a class, while the sub-figure (b) illustrates these abstractions with visual rules.

Figure 9 demonstrates the distribution of codebook symbols on a Poincare disk. The symbols from  $\zeta^0$  are spread along the circumference of the disk, while the symbols from  $\zeta^1$  and  $\zeta^2$  are distributed inside the disk, maintaining the hierarchy. Finally, Figure 10 demonstrates the class-level abstraction tree for class 'cat' and 'dog' in the AFHQ dataset. We can observe distinctions between symbols sampled and abstracted to form the class trees.

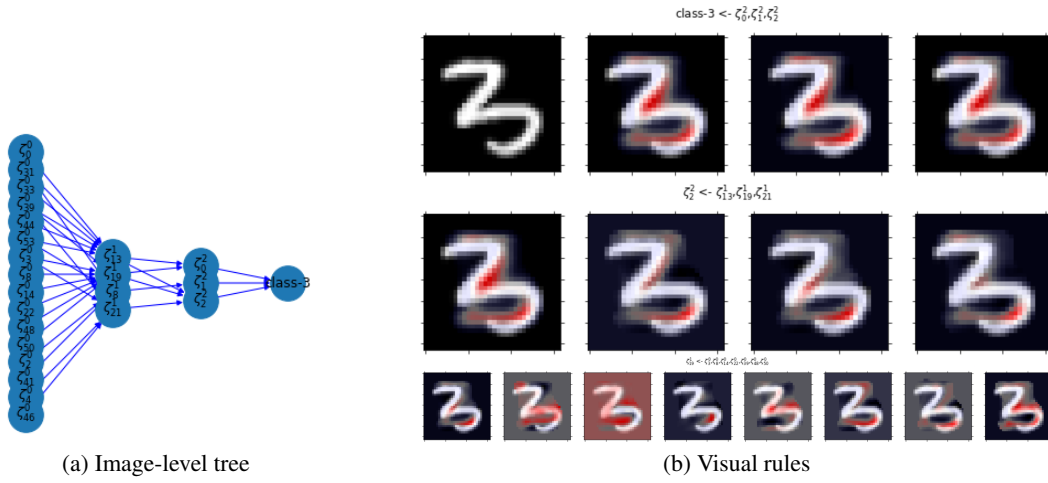


Figure 7: This figure describes the explanations obtained using our proposed framework on the MNIST classifier for class '3', with hierarchical rules:  $class3(x) \leftarrow \zeta_0^2(x), \zeta_1^2(x), \zeta_2^2(x)$ , where  $\zeta_2^2(x) \leftarrow \zeta_{13}^1(x), \zeta_{19}^1(x), \zeta_{21}^1(x)$ , and  $\zeta_{19}^1(x) \leftarrow \zeta_3^0(x), \zeta_8^0(x), \zeta_{14}^0(x), \zeta_{22}^0(x), \zeta_{48}^0(x), \zeta_{50}^0(x)$

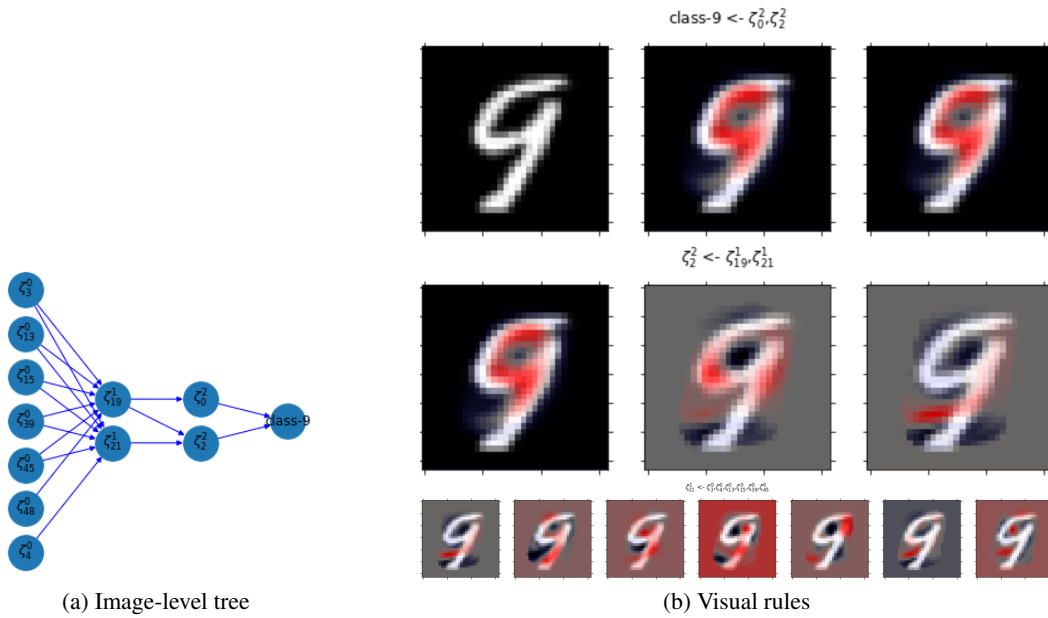


Figure 8: This figure describes the explanations obtained using proposed framework on the MNIST classifier for class '9', with hierarchical rules:  $class9(x) \leftarrow \zeta_0^2(x), \zeta_2^2(x)$ , where  $\zeta_2^2(x) \leftarrow \zeta_{19}^1(x), \zeta_{21}^1(x)$ , and  $\zeta_{21}^1(x) \leftarrow \zeta_3^0(x), \zeta_4^0(x), \zeta_{13}^0(x), \zeta_{15}^0(x), \zeta_{45}^0(x)$



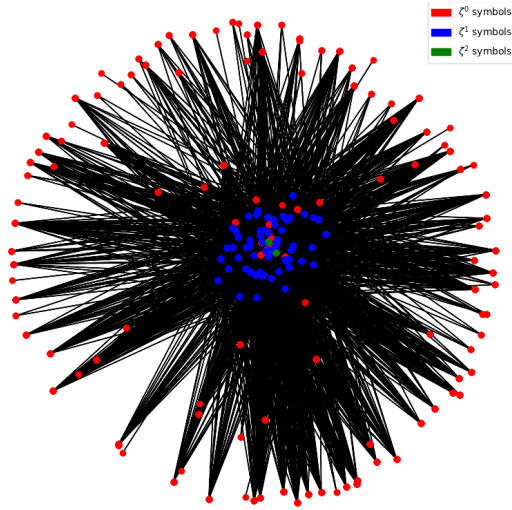


Figure 9: Poincare embedding of discrete symbols obtained for the AFHQ classifier. Here, red, blue, and green nodes indicate symbols from  $\zeta^0$ ,  $\zeta^1$ ,  $\zeta^2$  layers abstraction.

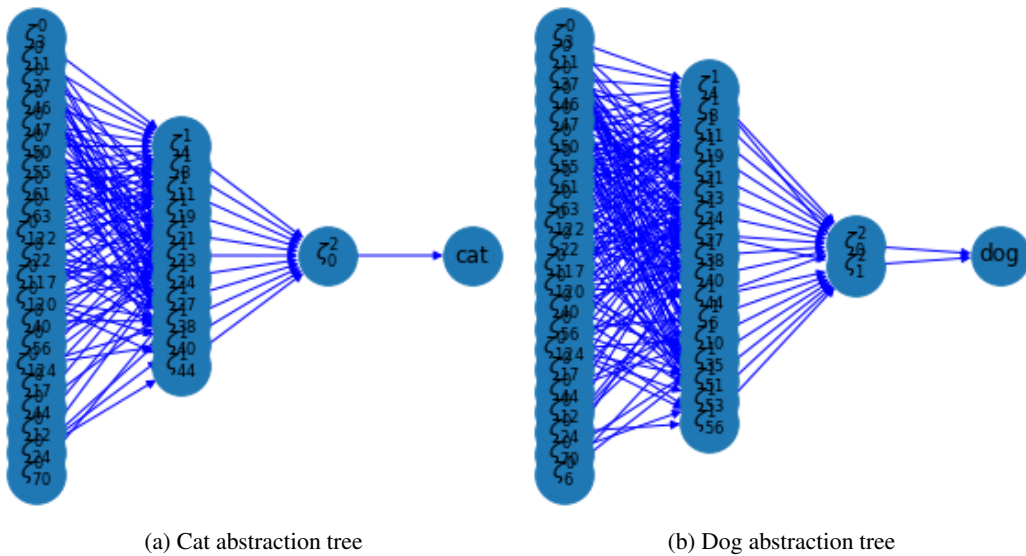


Figure 10: This figure describes the difference between class-level trees for 'cat' and 'dog' class, illustrating the difference in symbols sampled from  $\zeta^0$ ,  $\zeta^1$ , &  $\zeta^2$  in abstracting a particular class.

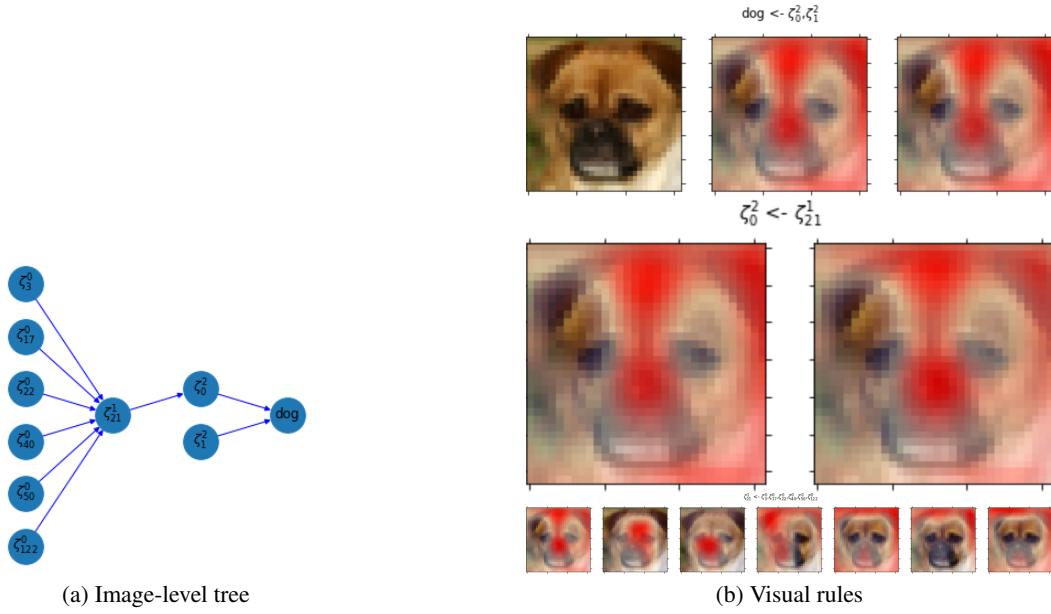


Figure 11: This figure describes the explanations obtained using our proposed framework for the AFHQ classifier for class dog, with hierarchical rules:  $dog(x) \leftarrow \zeta_0^2(x), \zeta_1^2(x)$ , where  $\zeta_0^2(x) \leftarrow \zeta_{21}^1(x)$ , and  $\zeta_{21}^1(x) \leftarrow \zeta_3^0(x), \zeta_{17}^0(x), \zeta_{22}^0(x), \zeta_{40}^0(x), \zeta_{122}^0(x), \zeta_{50}^0(x)$

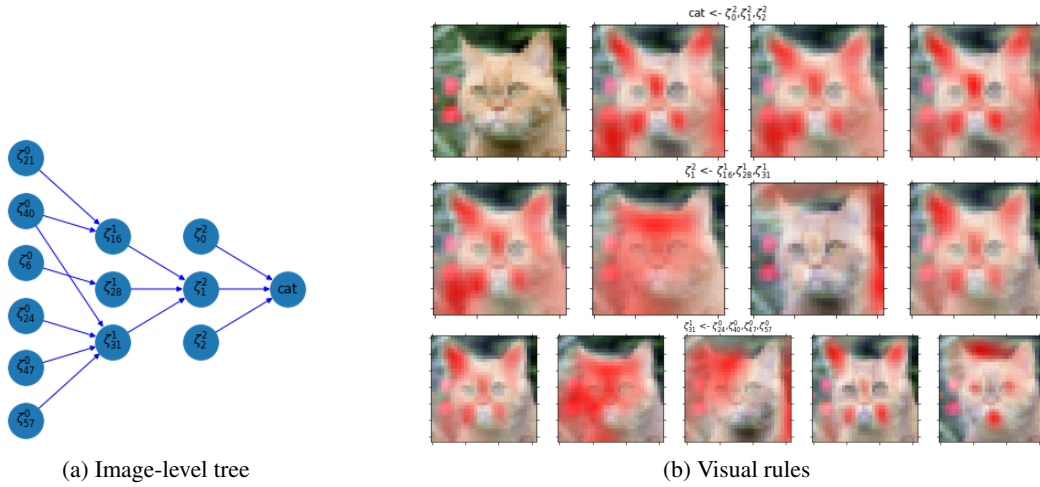


Figure 12: This figure describes the explanations obtained using our proposed framework for the AFHQ classifier classifying class 'cat' (ablation with 3 symbols in the final codebook of the hierarchy), with hierarchical rules:  $cat(x) \leftarrow \zeta_0^2(x), \zeta_1^2(x), \zeta_2^2(x)$ , where  $\zeta_1^2(x) \leftarrow \zeta_{16}^1(x), \zeta_{31}^1(x), \zeta_{28}^1(x)$ , and  $\zeta_{31}^1(x) \leftarrow \zeta_{24}^0(x), \zeta_{40}^0(x), \zeta_{57}^0(x), \zeta_{47}^0(x)$ .